Hybrid Plasma Catalysis-Thermal System for Non-oxidative Coupling of Methane to Ethylene and Hydrogen

Rui Liu,[1] Eduardo Morais,[2] Dongxing Li,[1] Pengfei Liu,[3] Qian Chen,[1] Shangkun Li,[2] Li Wang,[3] Xiaoxia Gao,[4] Annemie Bogaerts,[2] Hongchen Guo[1*] and Yanhui Yi[1*]

[1]State Key Laboratory of Fine Chemicals, Frontier Science Center for Smart Materials, School of Chemical Engineering, Dalian University of Technology, Dalian 116024, Liaoning, China

[2]Research group plasmaNT, Department of Chemistry, University of Antwerp, Universiteitsplein 1, BE-2610 Wilrijk-Antwerp, Belgium.

[3]College of Environmental Sciences and Engineering, Dalian Maritime University, Dalian 116026, Liaoning, China

[4]Instrumental Analysis Center, Dalian University of Technology, Dalian, 116024, P.R. China.

*Corresponding Author: hongchenguo@163.com; yiyanhui@dlut.edu.cn

1. Experiment

1.1 Experimental setup

The experimental framework, as illustrated in Figure S1, is segmented into two principal stages: stage 1 focuses on the plasma system with or without catalyst packing, whereas the subsequent stage 2 is dedicated to the thermal system. The distance between Stage 1 and Stage 2 is connected by a 10 cm four-fluorine hose, which does not affect the reaction performance, as demonstrated in our previous study. The input flow rate of the feedstock was maintained at 20 mL/min, adhering to a CH_4 to Ar ratio of 1:1, meticulously regulated by dual gas flow controllers. Stage 1 utilized a cylindrical DBD reactor, which encompasses a quartz tube featuring a 1 mm wall thickness serving as the dielectric barrier, and an inner diameter of 14 mm. Encasing the quartz tube, a stainless steel spiral wire, extending 15 cm in length, was meticulously coiled to function as the grounding electrode. In addition, a stainless-steel electrode, with a 2 mm outer diameter, was centrally positioned within the core of the quartz tube, acting as the High Voltage (HV) electrode. 4.3 g Pt/ZrO_2 catalyst was packed in DBD reactor of Stage 1 in plasma+Pt/ZrO_2 (+T) system. The residence time for stage 1 was calculated to be 67.8 s. Stage 2 is constructed around a quartz tube, having a residence time of 19.1 s, coupled with a heating furnace, integral for achieving precise temperature regulation.

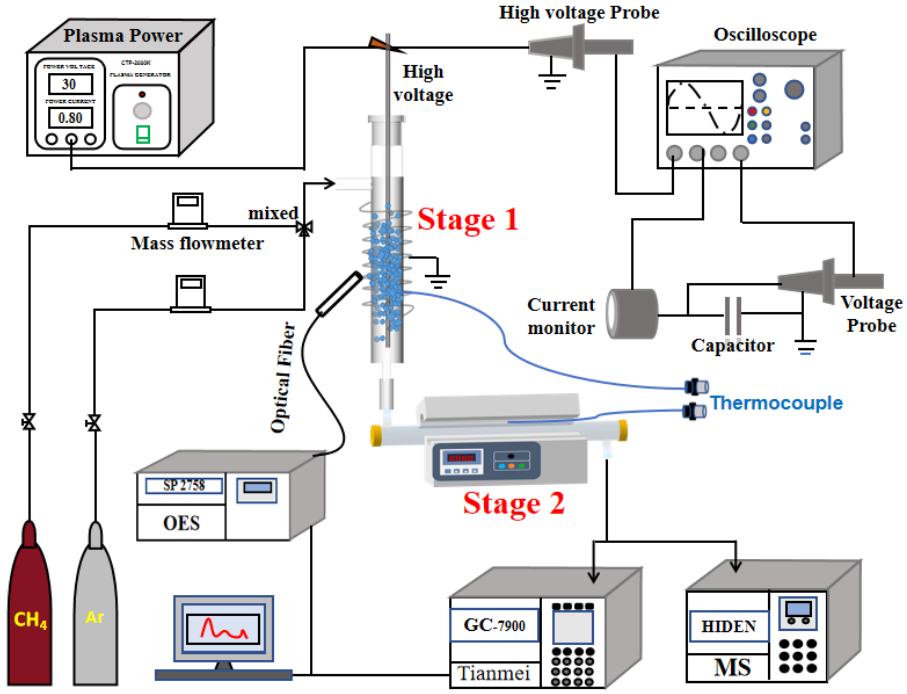

Figure S1. Schematic diagram of the experimental setup for NOCM through a plasma catalysis-thermal system.

The reactor from Stage 1 was energized using a sinusoidal AC power supply (Suman, CTP-2000K), which was linked to a transformer, stabilizing the voltage between 10 to 12 kV and securing the discharge frequency (*f*) at 13.8 kHz. To scrutinize the electrical parameters, a digital oscilloscope

(Tektronix, DPO 3012) was employed. Voltage at the plasma reactor was obtained through a high voltage probe (1000:1, P6015A, Tektronix), while the voltage across a 0.1 μF capacitor (C_m) was determined using a voltage probe (10:1, TPP0101, Tektronix) attached on either side of the capacitor. Furthermore, a current probe (Pearson 6585) was affixed to the ground electrode to ascertain the current traversing the DBD plasma reactor. Analysis of the gas-phase reactive species was carried out by optical emission spectroscopy (OES), through the wall of the quartz tube. Emission of excited species in the range of 200-1100 nm was collected by an optical fiber.

1.2 Product analysis

In this study, we conducted online analysis of the exhaust gases using a mass spectrometer (MS, HIDEN DECRA) set to Faraday detection mode, complemented by an online gas chromatograph (GC, Tianmei GC7900). The GC was equipped with an FID detector with a PLOT column (Al_2O_3, 50 m × 0.53 mm × 25 μm) for the effluent gases (CH_4, C_2H_2, C_2H_4, C_2H_6, C_3H_6, C_3H_8, i-C_4H_8, and n-C_4H_{10}) and a TCD detector with a TDX-01 column (2 m × 3 mm) for H_2. We determined the concentrations of various chemical species employing the external standard method, establishing standard curves from calibrated gas mixtures. It is critical to highlight that higher hydrocarbons, i.e., C_5 or higher, were classified as "coke" because their concentrations were below the detection limit of the gas chromatograph. The change of gas flow rate after the reaction was measured using a flow meter, which is needed to quantitatively analyze the gas composition, and to achieve the exact conversion (CH_4) and gaseous products selectivity, i.e, to account for gas expansion or contraction. To evaluate the efficiency of the CH_4 conversion process along with the selectivity and yield of gas-phase products, and coke selectivity, we applied specific equations.The selectivity formulas incorporate a molar carbon coefficient multiplier for calculating the selectivity of C_xH_y compounds and a 0.5 multiplier for H_2. This approach ensures that the selectivity calculations accurately reflect the stoichiometric distribution of carbon and hydrogen atoms, providing a more precise and meaningful representation of the reaction outcomes. The selectivity and yield calculations for C_xH_y used in this study are consistent with most reported literature. Therefore, the results can be compared with other published findings.

$$\text{Conversion of } CH_4\ (\%) = \frac{\text{Moles of } CH_4 \text{ converted}}{\text{Moles of } CH_4 \text{ input}} \times 100\%$$

$$\text{Selectivity of } C_xH_y\ (\%) = \frac{\text{Moles of } C_xH_y \text{ produced} \times x}{\text{Moles of } CH_4 \text{ converted}} \times 100\%$$

$$\text{Selectivity of } H_2\ (\%) = \frac{\text{Moles of } H_2 \text{ produced} \times 0.5}{\text{Moles of } CH_4 \text{ converted}} \times 100\%$$

$$\text{Selectivity of coke } (\%) = 1 - \sum_{x=2}^{x=4} \text{selectivity of } C_xH_y$$

$$\text{Yield (\%)} = \text{Conversion of } CH_4 \times \text{Selectivity of product} \times 100\%$$

$$\text{Carbon balance} = \frac{n_C^{out}}{n_C^{converted}} \times 100\%$$

The input power is calculated by Lissajous figure, as follow

$$P(W) = f \times C_m \times S$$

Where S is the area of the Lissajous figure.

The energy cost (EC) is the energy required for the main product, and is expressed as:

$$EC(kJ/mol) = 2 \times SEI/(\text{Conversion} \times \text{Main product selectivity}) \text{ [kJ/mol]}$$

The specific energy input (SEI) is calculated using the following equation,

$$SEI\ (kJ/mol) = \frac{22.4\ L/mol \times 60 \times (P_1 + P_2)(W)}{F(ml/min)}$$

Where P(W) is the input power, P_1 is the power of Stage 1 from the plasma discharge power and the P_2 is the power of Stage 2 from the power meter for heating zone. F(ml/min) is the flow rate of the feed gas, and 60 is the conversion from minutes to seconds. Therefore, SEI is the sum of Stage 1 and Stage 2, while the energy costs pertain to the entire reaction system.

1.3 Catalyst preparation

We utilized commercial ZrO_2, CeO_2, and γ-Al_2O_3 powders (Sigma-Aldrich, 99.99% purity) to prepare platinum-supported catalysts, and the N_2 Physicochemical properties was shown in Table S7. For the ZrO_2 supports, the catalysts were synthesized by impregnating ZrO_2 powder with an aqueous solution of chloroplatinic acid hexahydrate ($H_2PtCl_6 \cdot 6H_2O$, Aldrich, 99.99% purity), achieving nominal Pt loading of 0.1-5 wt% on ZrO_2. This mixture was stirred at room temperature for 30 minutes. Following overnight drying at 120 °C, the samples were calcined under an air flow at 600 °C for 5 hours, employing a linear heating ramp of 10 °C/min to attain the target temperature. Once cooled to room temperature, the catalysts, designated as 0.1wt %, 0.5wt %, 1wt %, 3wt %, and 5wt % Pt/ZrO_2, were stored under dry conditions. Similarly, 0.5 wt% Pt/CeO_2 and 0.5wt% Pt/γ-Al_2O_3 catalysts were prepared following the same procedure.

2. NOCM performances over Pt-based catalysts.

Table S1 XRF results for Pt/ZrO_2 catalysts

Catalyst	PtO（%）
0.5%Pt/ZrO_2	0.496
1%Pt/ZrO_2	0.997
3%Pt/ZrO_2	3.102
5%Pt/ZrO_2	4.904

Table S2. Textural properties of Pt/ZrO_2 catalysts

Catalyst supports	BET surface area ($m^2\ g^{-1}$)	Average pore diameter (nm)	Pore volume ($cm^3\ g^{-1}$)
3%Pt/ZrO_2-Fresh	14.3	39.5	0.0033
3%Pt/ZrO_2-Spent	12.8	31.4	0.0018
5%Pt/ZrO_2-Fresh	14.7	27.2	0.0016
5%Pt/ZrO_2-Spent	12.9	30.7	0.0007

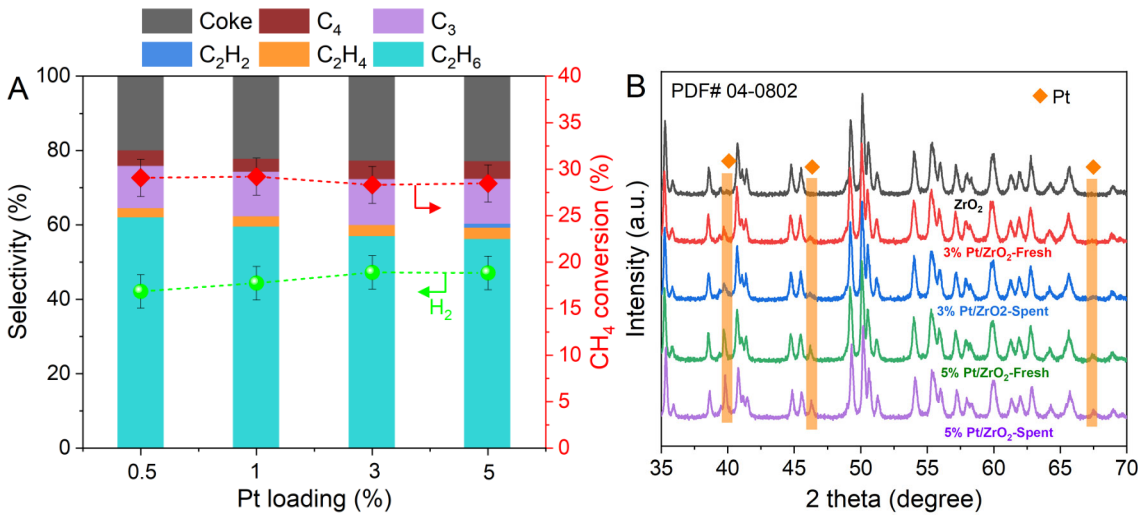

Figure S2. Effect of Pt loadings on NOCM results. (A) reaction results, (B) XRD patterns.

Figure S2A depicts the CH_4 conversion and product selectivity during NOCM using Pt/ZrO_2 catalysts with various Pt loadings. The actual Pt loading was confirmed by XRF (Table S1). Optimal performance in C_2H_6 production and enhanced resistance to coke formation were observed in a DBD plasma reactor equipped with a catalyst containing 0.5% Pt/ZrO_2. We hypothesize that lower Pt loading (0.1%) are insufficient to adsorb CH_4 or CH_3 radicals, thereby inadequately promoting CH_4 dissociation and C-C coupling. Conversely, higher Pt loadings (3-5%) are prone to facilitate sintering

and agglomeration, which has been confirmed by XRD and N_2 adsorption-desorption results. Compared to the Pt/ZrO_2-fresh catalyst, the XRD diffraction peaks of Pt become narrower and higher in the Pt/ZrO_2-spent catalyst, as shown in Figure S2B, indicating grain growth and the occurrence of sintering. Moreover, both the BET surface area and pore volume decrease in the spent Pt/ZrO_2 catalyst (Table S2), further indicating that sintering has occurred.

Table S3 Physicochemical properties of the metal oxides supports

Catalyst supports	BET surface area (m^2 g^{-1})	Average pore diameter (nm)	Pore volume (cm^3 g^{-1})	Dielectric constant
CeO_2	16.4	8.8	0.056	26
γ-Al_2O_3	138.6	11.4	0.408	9-10
ZrO_2	11.4	33.3	0.056	17

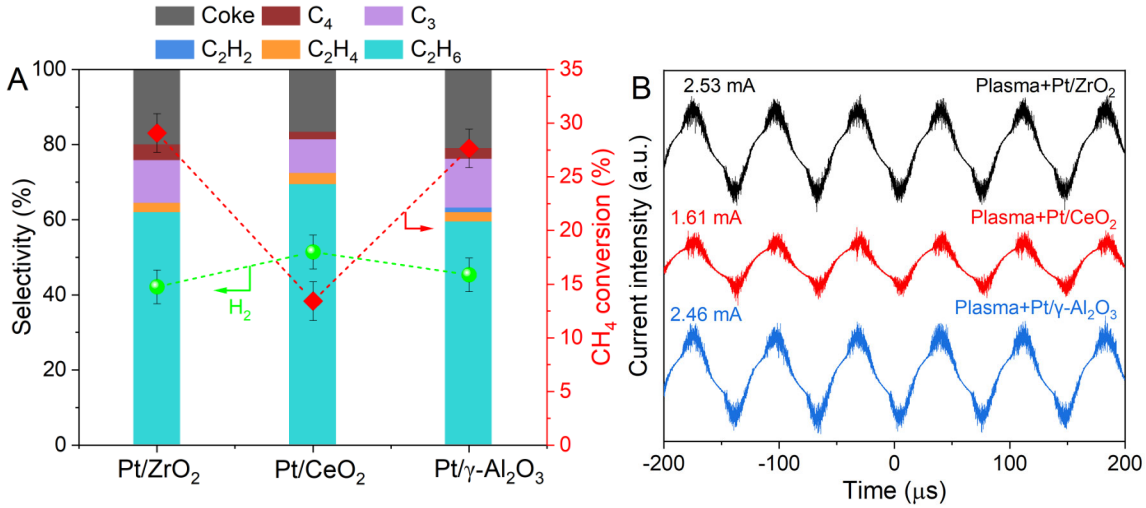

Figure S3. (A) CH_4 conversion and product selectivity in NOCM using 0.5% Pt supported on ZrO_2, CeO_2, and γ-Al_2O_3. (B) Current curves for different catalysts system.

Figure S3 (A) depicts the CH_4 conversion and product selectivity in NOCM using Pt-based catalysts on three different supports. It is clear that C_2H_6 is the predominant product, with the Pt-based catalysts promoting its formation more effectively than systems utilizing plasma alone (Figure 1 in the main paper). The Pt/ZrO_2 packing achieves the highest CH_4 conversion. Although the selectivity for C_2H_6 in the Pt/CeO_2 system exceeds that of the Pt/ZrO_2 packing, the yield of C_2H_6 follows the performance ranking: Pt/ZrO_2 > Pt/Al_2O_3 > Pt/CeO_2. These differences are primarily due to the properties of the supports, the characteristics of the metal active sites, and the interactions between the support and the metal. The low CH_4 conversion of Pt/CeO_2 is attributed to its low BET surface area and small pore size of CeO_2 support (Table S3), which limit the contact efficiency between reactants and active sites. Moreover, the dielectric constant of CeO_2 is higher than that of γ-Al_2O_3 and ZrO_2, which allows CeO_2 support to store more electrical energy and produce greater polarization under the same applied voltage. This polarization results in an induced electric field

within the material that opposes the direction of the external electric field, partially canceling out the applied electric field and consequently reducing the overall electric field strength. In contrast, γ-Al_2O_3, with its high specific surface area and large pore volume, facilitates better diffusion and contact of reactants, leading to a higher CH_4 conversion. Although ZrO_2 has a lower specific surface area, its larger pore size aids in gas diffusion. Moreover, ZrO_2 can anchor Pt, which is beneficial for CH_4 dissociation at Pt sites, thereby further enhancing CH_4 conversion in the case of Pt/ZrO_2 catalyst. Taking all aspects into consideration, the yield of C_2H_6 follows the order: Pt/ZrO_2 > Pt/γ-Al_2O_3 > Pt/CeO_2. This can also be confirmed by Figure S3 (B) that the discharge current of Pt/ZrO_2 is higher than Pt/γ-Al_2O_3 and Pt/CeO_2, and Pt/CeO_2 packing shows the lowest discharge current.

3. NOCM performances with different feed gas ratio

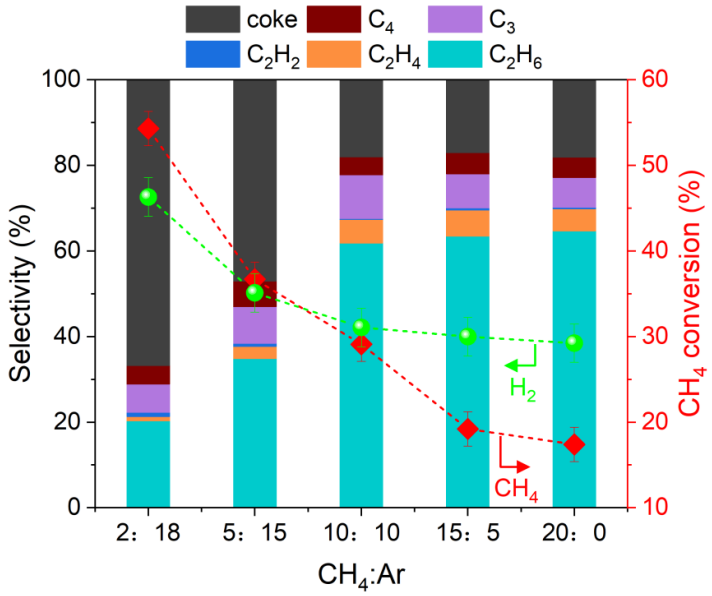

Figure S4. CH_4 conversion and product selectivity for different feed gas ratio in plasma+Pt/ZrO_2 system

In Figure S4, as the CH_4/Ar ratio increases from 2:18 to 20:0, CH_4 conversion and H_2 selectivity decrease, while C_2H_6 selectivity first increases and then stabilizes. The yield of C_2H_6 reaches its optimal value at a CH_4/Ar ratio of 10:10 ml/min. Therefore, the input feed gas should be maintained at a CH_4 to argon ratio of 1:1. This phenomenon occurs mainly because CH_4 conversion can be influenced by energy transfer from excited states, such as the Penning effect, or by charge transfer from ionic states of noble gases. The energy transferred kinetically by excited noble gas atoms to CH_4 molecules can cause subsequent CH_4 dissociation,[1-3] leading to higher CH_4 conversion with high content of argon.

4. NOCM performances comparison with literature

Table S4. Comparison of this study with some representative results from literature for NOCM

Catalyst	CH_4 conversion (%)	C_2H_4 selectivity (%)	C_2H_4 yield (%)	Reference
PtSn/H-ZSM-5	0.06	0.95	0.057	[4]
GaN/SBA15	0.32	0.71	0.226	[5]
Mo_2C[B]ZSM-5	1.18	0.89	1.061	[6]
Fe-Mo/HZSM-5	2.19	0.36	0.792	[7]
Pt/Al_2O_3	8.20	0.12	0.984	[8]
MFM-300(Fe)	10.03	0.58	5.834	[9]
-	16.86	0.64	10.866	[10]
Ni-Ti	20.20	0.55	11.108	[11]
Pt/ZrO_2	27.60	0.66	18.188	this Study
Pt/CeO_2-SAC	39.00	0.06	2.340	[12]
Fe©SiO_2	48.08	0.48	23.204	[13]
PtCe/CuX-ZY	73.50	0.24	17.566	[14]

Table S5 NOCM to C_2H_4 and H_2 results in different reaction systems.

Systems	CH_4 conversion (%)	Selectivity(%)				Yield (%)			
		C_2H_6	C_2H_4	Coke	H_2	C_2H_6	C_2H_4	Coke	H_2
plasma alone	26.6	43.0	3.6	24.0	49.1	11.4	1.0	6.4	13.1
plasma + T	22.5	6.5	60.1	26.0	62.4	1.5	13.5	5.9	14.0
plasma + Pt/ZrO_2	29.1	61.9	5.5	18.0	42.1	18.0	1.6	5.2	12.3
plasma+Pt/ZrO_2+T	27.6	5.8	65.9	21.5	60.5	1.6	18.2	5.9	16.7

5. Discharge voltage and thermal cracking temperature

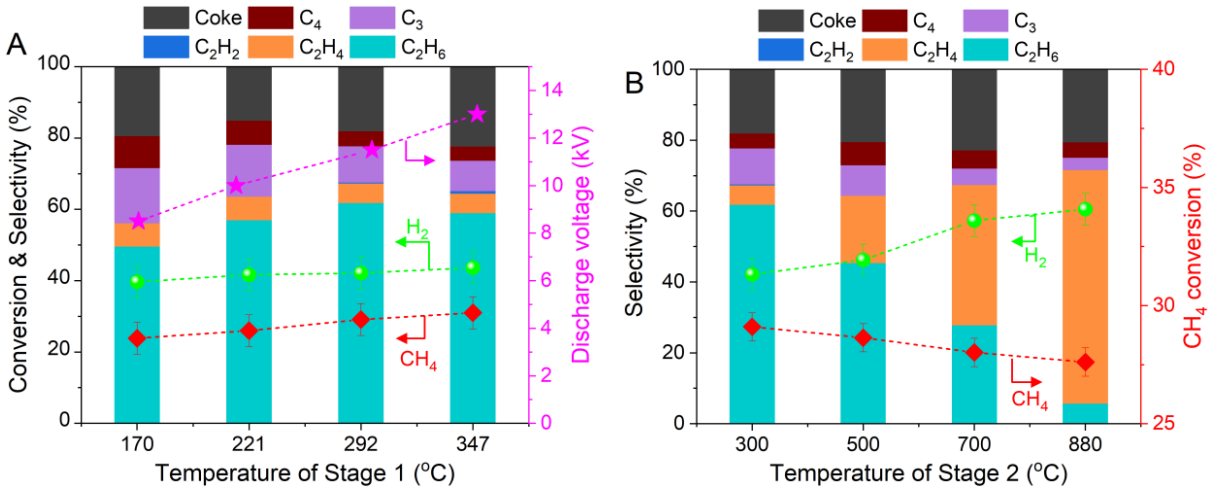

Figure S5. CH_4 conversion and product selectivity as functions of (A) temperature of stage 1 in plasma+Pt/ZrO_2 system, and (B) temperature of stage 2 in plasma+Pt/ZrO_2+T system.

In Figure S5, the temperature in Stage 1 is primarily influenced by the Stage 1 DBD plasma discharge voltage. CH_4 conversion increases with the rising temperature in Stage 1. In the plasma + Pt/ZrO_2 system, C_2H_6 selectivity increases to a maximum value at 292 °C and then decreases. The temperature in Stage 2 is controlled by the heating furnace, which affects C_2H_4 selectivity. As the temperature in Stage 2 increases, CH_4 conversion and C_2H_6 selectivity decrease, while C_2H_4 selectivity increases.

6. Thermodynamic calculations

The chemical composition at a specific temperature was calculated by minimizing the Gibbs free energy to find the thermodynamic equilibrium of all considered species. The species considered in this analysis are as follows: C, CH, CH_2, CH_3, CH_4, C_2, C_2H, C_2H_2, C_2H_3, C_2H_4, C_2H_5, C_2H_6, C_3H_5 allyl, C_3H_6, C_3H_7 (n-propyl), C_3H_7 (i-propyl), C_3H_8, C_4H_{10} (n-butane), C_4H_{10} (isobutene), C_6H_6, H, H_2 and C(s). The calculations were performed with 100% CH_4 (the inclusion of argon does not alter the results, since it does not dissociate) and initiated at 298.15 K and 1 bar. We scanned a temperature range between 298.15 and 1600 K. During the scan, CH_4 is initialized and equilibrated at each temperature and the composition of the new mixture (as molar fraction) is assessed as a function of temperature, when thermodynamic equilibrium is reached. The calculations were carried out using the free tool Cantera.[15] Cantera utilizes the NASA9 [16] polynomials and the VCS algorithm [17] to evaluate the Gibbs free energy.

The compositions as a function of temperature are presented in Figures S6 and Figure S7.

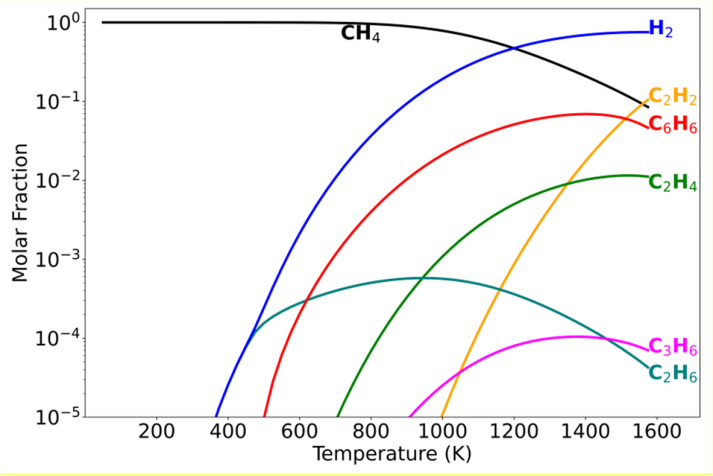

Figure S6. Gas-phase equilibrium composition at 1 bar with an initial composition of 1 mole of CH_4 under the assumption that there is no formation of solid-phase carbon – C(s). Species with molar fraction below 10^{-5} are not shown on this graph for clarity and readability.

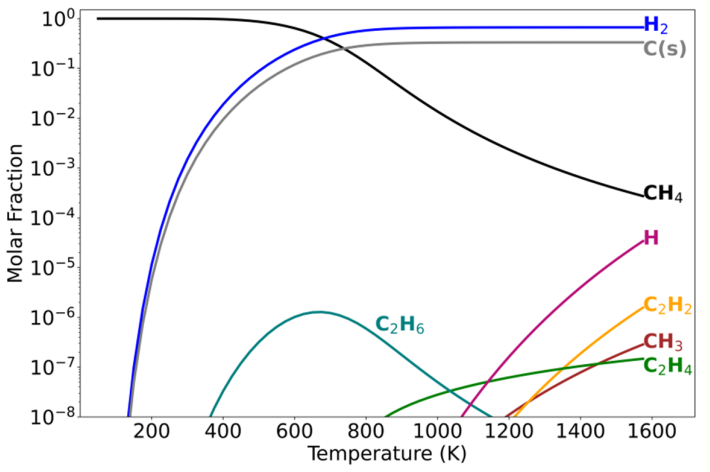

Figure S7. Calculated gas-phase equilibrium composition at 1 bar with an initial composition of 1 mole of CH_4 under the assumption that solid-phase carbon – C(s) is formed in equilibrium with the gas-phase. Species with molar fraction below 10^{-8} are not shown on this graph for clarity and readability.

Acrroding to the compositions as a function of temperature in Figure S6 and Figure S7. The CH_4 conversion and the selectivity of the main products are presented in Figure S8.

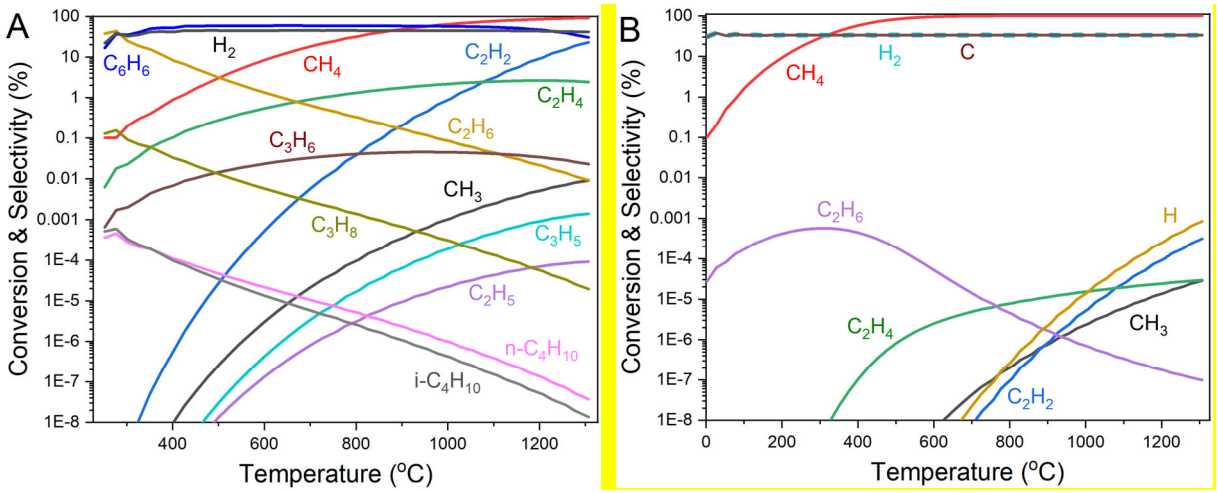

Figure S8. Thermodynamic equilibrium calculation of CH_4 pyrolysis, including CH_4 conversion and product selectivity for main species. (A) without Carbon (C), and (B) with C.

Figure S8 illustrates the conversion and selectivity of the main products as a function of temperature. In this thermodynamic calculation, coke products were excluded from Figure S8(A) to focus on the trends in C_xH_y hydrocarbons selectivity. Benzene (C_6H_6) is the primary product. Among the C_2 hydrocarbons, C_2H_6 predominates below 630 ºC, C_2H_4 between 630 ºC and 1100 ºC, and C_2H_2 above 1100 ºC. In Figure S8(B), which includes carbon (C) in thermodynamic calculations. C is the dominant product. The main C_2 products show a similar trend: C_2H_6 dominates below 750 ºC, C_2H_4 between 750 ºC and 1100 ºC, and C_2H_2 above 1100 ºC. These results align with the thermodynamic calculations excluding carbon. This indicates that at our reaction temperature (880 ºC), C_2H_4 is the main product in C_2 hydrocarbons.

7. Carbon balance

$$\text{Carbon balance} = \frac{n_c^{out}}{n_C^{converted}} \times 100\%$$

$$= \frac{n_{C2H6} + n_{C2H4} + n_{C2H2} + n_{C3} + n_{C4} + n_{\text{Carbon deposition}}}{n_c^{converted}} \times 100\%$$

Where $n_c^{converted}$ is the moles of CH_4 converted, n_c^{out} is moles of products in terms of carbon.

Take the results of NOCM in the case of plasma + Pt/ZrO_2 in Table 5 as an example:

$$n_c^{converted} = \frac{10\ \text{ml/min}}{22400\text{ml/mol}} \times 29.1\% = 1.298 \times 10^{-4}\text{mol/min}$$

$$n_{CxHy} = n_c^{cnnverted} \times S_{CxHy}$$

$$n_{C2H6} = n_c^{cnnverted} \times S_{C2H6} = 1.298 \times 10^{-4}\text{mol/min} \times 61.88\% = 8.039 \times 10^{-5}\text{mol/min}$$

$$n_{C2H4} = n_c^{cnnverted} \times S_{C2H4} = 1.298 \times 10^{-4}\text{mol/min} \times 5.47\% = 7.143 \times 10^{-6}\text{mol/min}$$

$$n_{C2H2} = n_c^{cnnverted} \times S_{C2H2} = 1.298 \times 10^{-4}\text{mol/min} \times 0.25\% = 3.247 \times 10^{-6}\text{mol/min}$$

$$n_{C3} = n_c^{cnnverted} \times S_{C3} = 1.298 \times 10^{-4}\text{mol/min} \times 10.19\% = 1.325 \times 10^{-5}\text{mol/min}$$

$$n_{C4} = n_c^{cnnverted} \times S_{C4} = 1.298 \times 10^{-4}\text{mol/min} \times 4.20\% = 5.455 \times 10^{-5}\text{mol/min}$$

According to the TGA results (Figure S19A), $n_{\text{Carbon deposition}}$ calculated as follow,

$$n_{Carbon\ deposition} = \frac{m \times \Delta Tg\%}{12\ g/mol \times 60\ min} = \frac{4.3\ g \times 0.17996\%}{12\ g/mol \times 60\ min} = 1.075 \times 10^{-5} mol/min$$

Where the mass of the reaction sample (m) is 4.3 g. Tg% represents the mass loss percentage as determined by thermogravimetric analysis (Figure S9A). Based on a comparison of the catalyst before and after the reaction in TGA-MS analysis, the temperature range for coke is identified to be between 200°C and 450°C (Figure S9B). The reaction time is 60 minutes.

$$\Delta TG\% = \Delta TG_{\text{Spent}} - \Delta TG_{\text{Fresh}} = (TG_{\text{Spent}-1} - TG_{\text{Spent}-2}) - (TG_{\text{Fresh}-1} - TG_{\text{Fresh}-2})$$

$$= 0.89643\% - 0.71647\% = 0.17996\%$$

$$n_c^{out} = 8.039 \times 10^{-5} mol/min + 7.143 \times 10^{-6} mol/min + 3.247 \times 10^{-6} mol/min + 1.325 \times 10^{-5} mol/min + 5.455 \times 10^{-6} mol/min + 1.075 \times 10^{-5} mol/min = 1.202 \times 10^{-4} mol/min$$

$$\text{Carbon balance} = \frac{1.202 \times 10^{-4}\text{mol/min}}{1.298 \times 10^{-4}\text{mol/min}} \times 100\% = 92.6\%$$

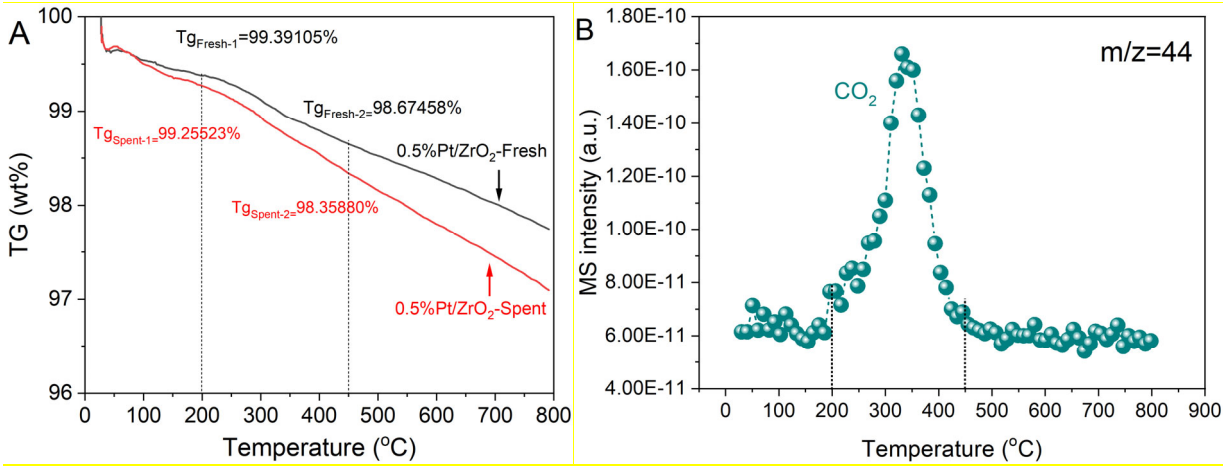

Figure S9. (A) TGA profiles, and (B) MS profiles (m/z=44) observed over fresh and spent 0.5%Pt/ZrO_2 catalyst

Figure S9A shows the thermogravimetric analysis (TGA) of fresh and spent 0.5% Pt/ZrO_2 catalysts at different temperatures. In the range of 0 to 100 ºC, both catalysts exhibit significant weight loss, primarily due to the evaporation of water and volatile organic compounds adsorbed on the catalyst surface. As the temperature increases, the weight of both catalysts gradually decreases. However, the spent catalyst shows slightly greater weight loss compared to the fresh catalyst, indicating the formation of carbon deposits on the surface and in the pores of the catalyst during the reaction.

The carbon balance did not reach 100% because small amounts of yellow oily substances appeared on the reactor walls, which were not detected by gas chromatography.

8. Coke images

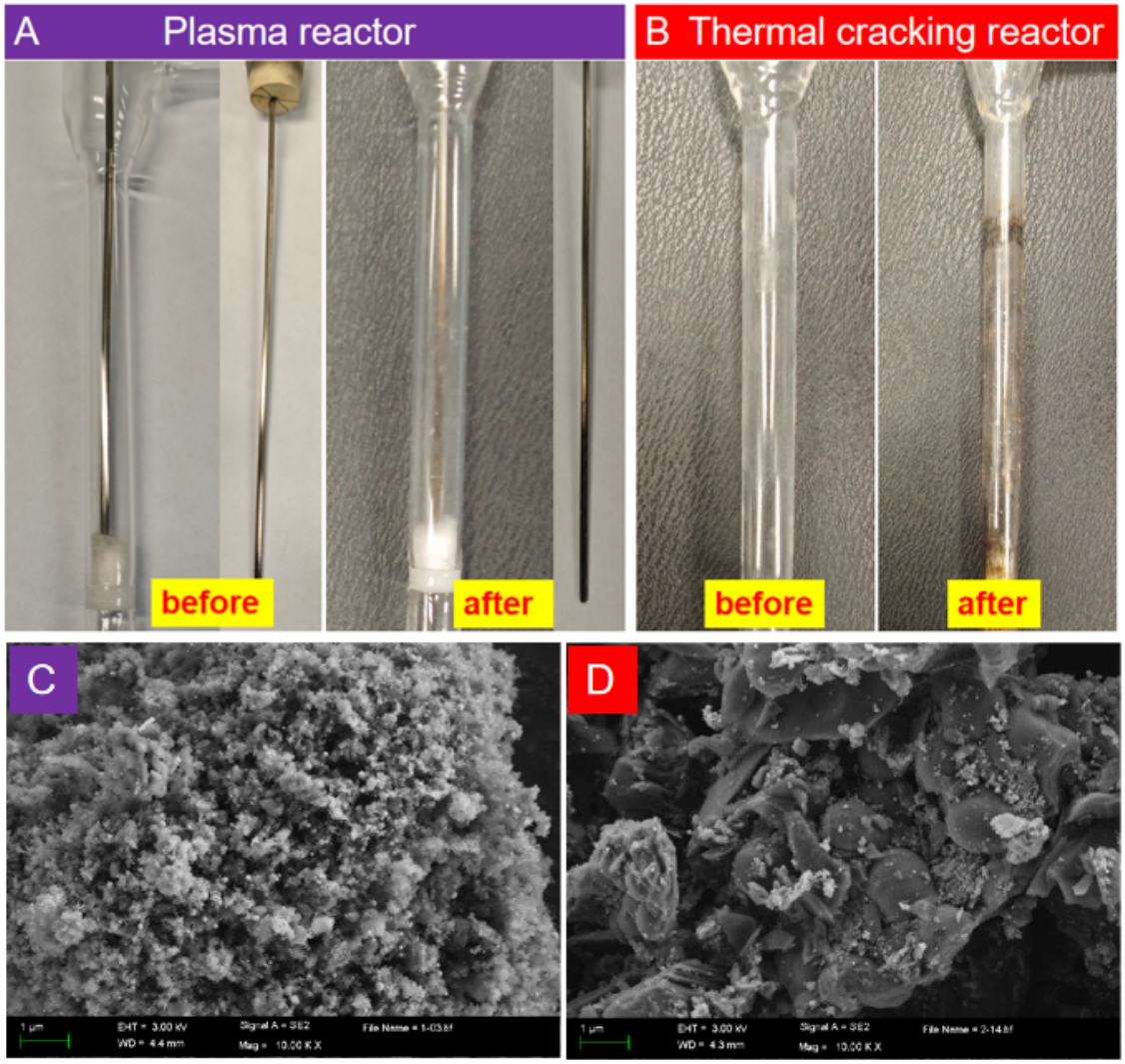

Figure S10. Reactor for (A) plasma zone, and (B)thermal cracking zone; SEM images for coke, (C) in plasma reactor, and (D) in thermal cracking reactor.

The images of the plasma reactor and the thermal cracking reactors are shown in Figure S10(A) and Figure S10(B), respectively. In Figure S10(A), compared with reactor before reaction, there is significant carbon deposition on the electrode in the reactor after NOCM reaction. In Figure S10(B), there is a slight carbon deposition on the wall of the thermal cracking reactor after NOCM reaction. Figure S10(C) and Figure S10(D) are SEM images of the carbon deposits in the plasma and thermal cracking reactor, respectively. In fact, in plasma alone system for NOCM reaction, with increasing the CH_4 conversion, the C_2 selectivity decreases, and the coke selectivity increases, which belong to a gas phase reaction. However, in the plasma+Pt/ZrO_2 system for NOCM reaction, the C_2 selectivity increases with increasing the CH_4 conversion and the decreasing of the coke, which implied that it belongs a catalyst surface effect for enhanced CH_4 conversion and C_2H_6 selectivity with Pt/ZrO_2 catalyst.

9. Stability evaluation of the NOCM reaction

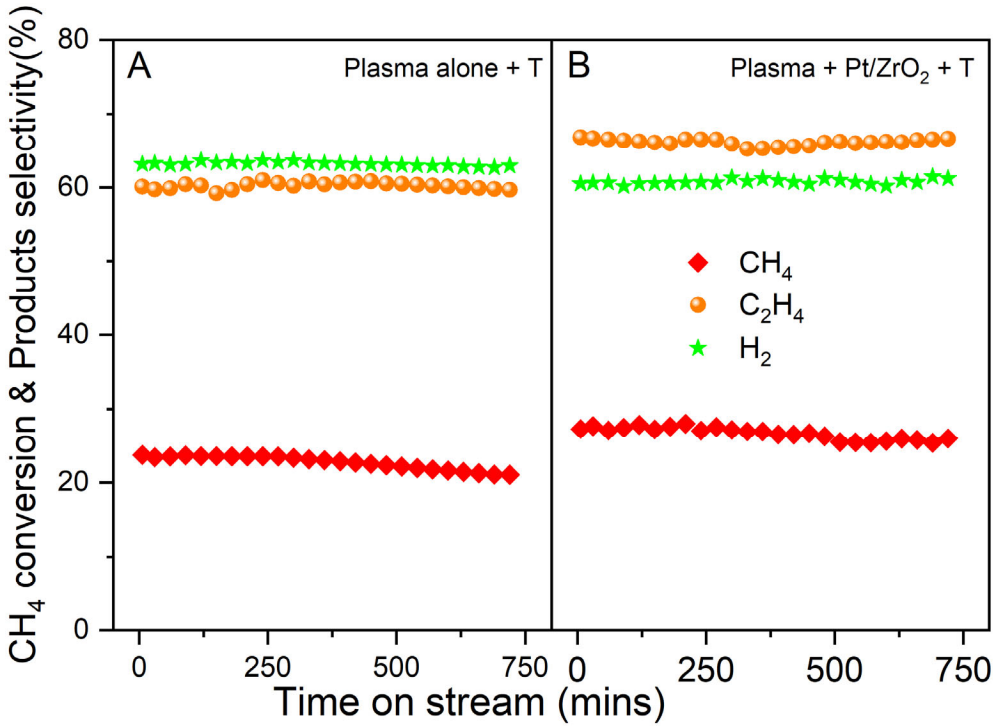

Figure S11. Performance of the NOCM reaction under (A) plasma alone+T system, and (B) plasma+Pt/ZrO_2+T system (T represents thermal cracking temperature is 880 ºC).

The stability tests for the NOCM of both "plasma alone+T" and "plasma+Pt/ZrO_2+T" systems were examined, as illustrated in Figure S11. Compared to the plasma alone+T system, the plasma+Pt/ZrO_2+T system exhibits a higher selectivity towards C_2H_4. This is attributed to the efficiency of the Pt/ZrO_2 packing in dissociating CH_4 to CH_3, which subsequently enhances C-C coupling, leading to the formation of C_2H_6. Subsequently, a greater quantity of C_2H_6 undergoes thermal cracking during Stage 2, resulting in the conversion to C_2H_4. The enhancement in CH_4 conversion can be attributed to the presence of Pt active sites likely facilitates the dissociation of CH_4, thus promoting the CH_4 conversion.

10. Peak area of products from GC profiles

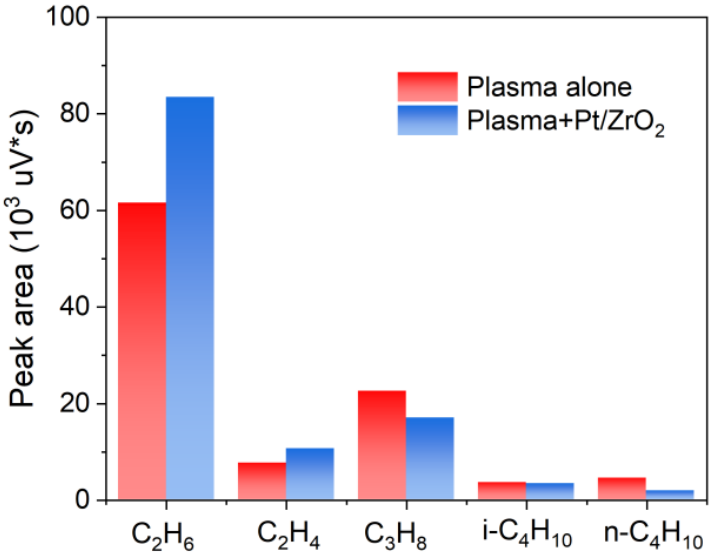

Figure S12. Peak area of reaction product from GC profiles.

Figure S12 shows the peak areas of the main products for NOCM in both the plasma alone system and the plasma+Pt/ZrO_2 system. Compared to the plasma alone system, the peak areas of C_2H_6 and C_2H_4 increase, while the peak areas of C_3 and C_4 decrease.

11. GC profiles of products from NOCM.

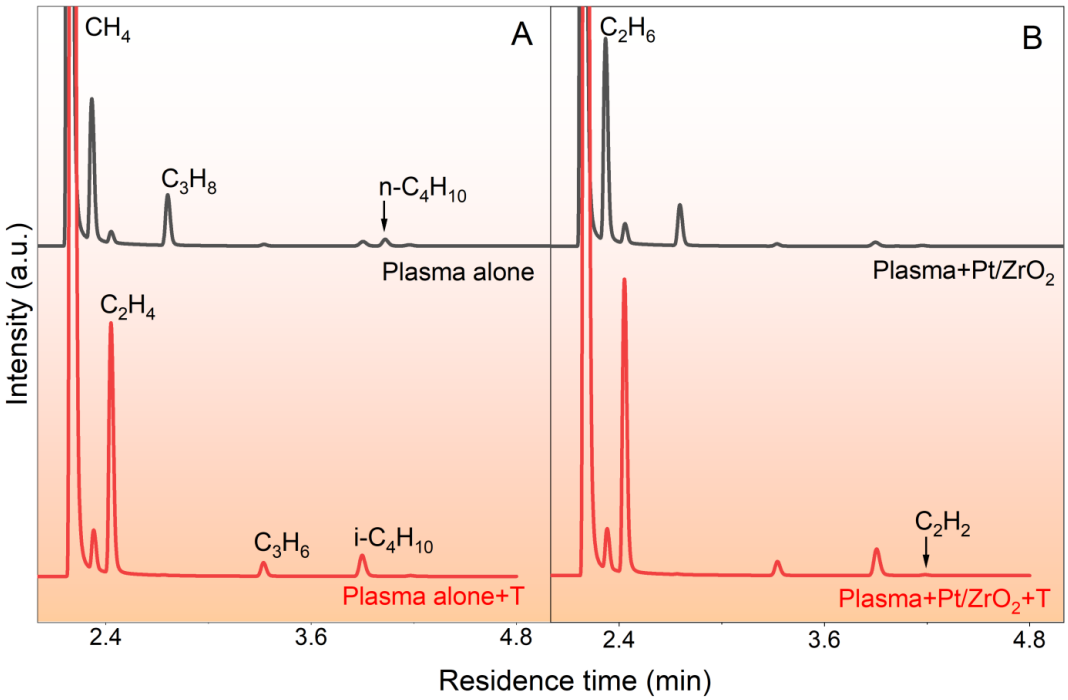

Figure S13. Gas chromatogram analysis of NOCM product distribution (A) comparing plasma alone and plasma alone + T, and (B) comparing plasma + Pt/ZrO_2 system and plasma+Pt/ZrO_2 + T system (T represents thermal cracking temperature is 880 ºC).

The chromatographic analysis of gas from the plasma alone, plasma alone+T, plasma+Pt/ZrO_2, and plasma+Pt/ZrO_2+T systems is presented in Figure S13. This analysis reveals that C_2H_6 is the primary product in both the plasma alone and the plasma+Pt/ZrO_2 systems, with the latter demonstrating enhanced efficacy in facilitating C-C coupling to produce C_2H_6. Conversely, in the plasma alone+T and plasma+Pt/ZrO_2+T systems, C_2H_4 emerges as the predominant product, with the plasma+Pt/ZrO_2+T system exhibiting a notably higher intensity of C_2H_4. These results more directly indicate that the Pt/ZrO_2 catalyst is more effective at generating C_2H_6 and reducing C_3H_8 production, whereas the thermal cracking occurring in Stage 2 is more likely to produce C_2H_4. The selectivity of C_3 and C_4 hydrocarbons may be improved from three aspects. Firstly, in a plasma-catalysis system, the addition of metal catalysts are potential to promote the formation of C_3 and C_4 hydrocarbons. Secondly, in a two-stage plasma thermal system, DBD plasma conversion of CH_4 primarily produces alkanes (C_2H_6, C_3H_8, C_4H_{10}). C_3H_8 is predominantly formed via the reaction $CH_3\cdot + C_2H_5\cdot \rightarrow C_3H_8$, while C_4H_{10} is mainly produced from the reaction $C_2H_5\cdot + C_2H_5\cdot \rightarrow C_4H_{10}$.[18] C_3H_8 and C_4H_{10} thermally decompose above 500 ºC,[1] therefore, the temperature in the thermal zone should not exceed 500 ºC. Finally, catalysts that can convert C_2H_6 into C_3H_8 and C_4H_{10} can be added in the thermal zone.

12. Energy consumption for C_2H_4 production

Table S6 The energy cost for the production of C_2H_4

Reaction system	Energy cost for production of C_2H_4 (kJ/mol)	Reference
plasma alone	344320	This study
plasma + T	27498	This study
plasma + Pt/ZrO_2	215200	This study
plasma+Pt/ZrO_2+T	20397	This study
Nanosecond pulsed discharge	2020	[19]
Nanosecond pulsed discharge+Pd-based	1642	[20]

As shown in Table S6, compared to Ref[21] and Ref [20], the energy costs in our study are higher by more than 20 MJ/mol C_2H_4. This difference can be attributed to several factors: Firstly, gas flow rate: In Ref [19] and Ref [20], the gas flow rate was 200 sccm, whereas in our study it was 20 sccm. A higher gas flow rate results in a smaller specific energy input (SEI) and thus lower energy consumption. By increasing the gas flow rate and optimizing the reaction, the energy consumption could be significantly reduced in our study. Secondly, the advantage of using a nanosecond pulsed power supply is its lower energy consumption.[21, 22] We plan to leverage this benefit in future work. Finally, in Ref [21,] the reaction was conducted at high pressure (5 bar), while Ref [20] utilized a complex reactor design that is not suitable for industrial applications.

13. HAADF-STEM-EDX mapping images of Pt/ZrO_2 catalysts

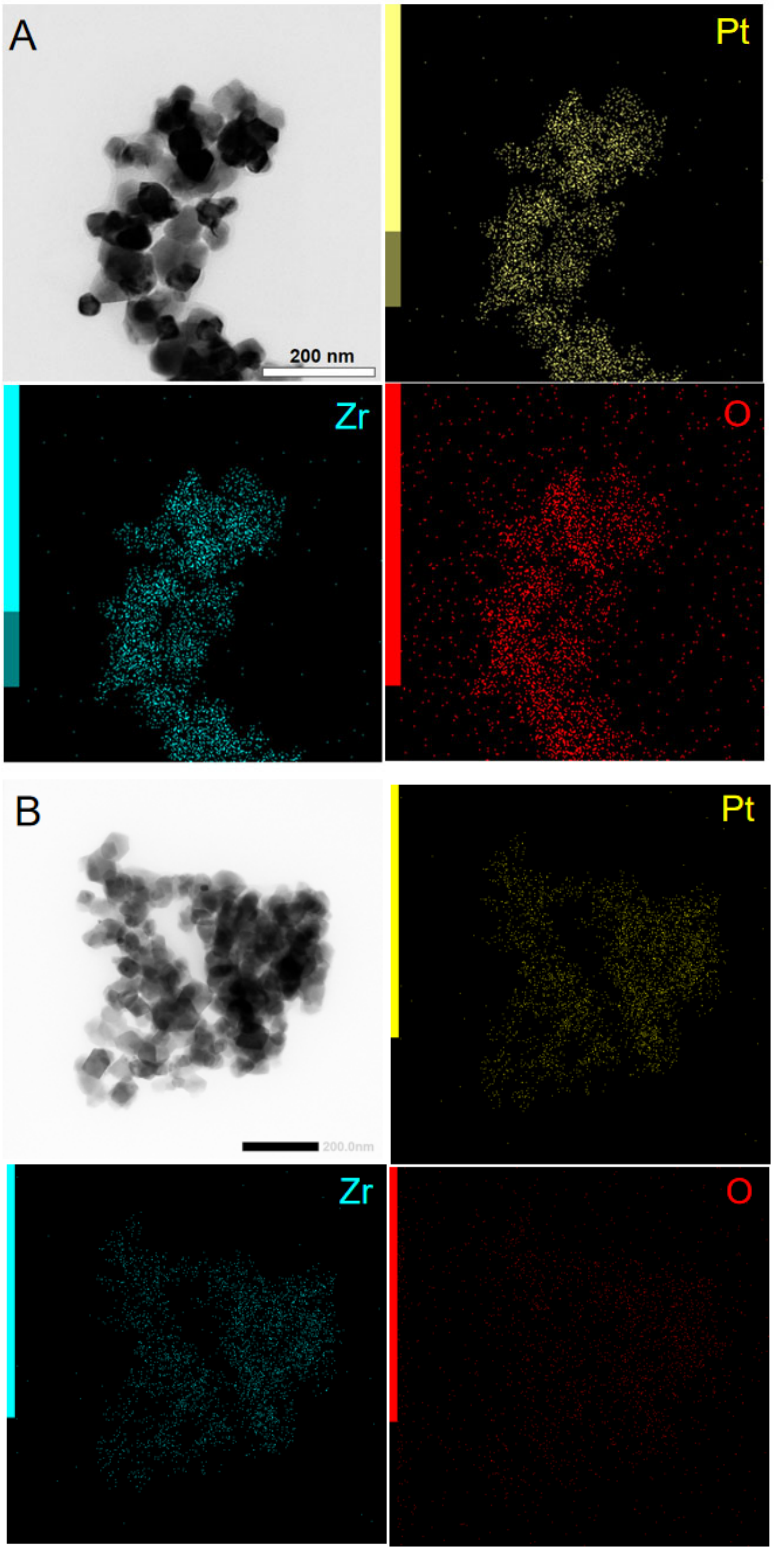

Figure S14. HAADF-STEM-EDX element-mapping analyses of (A) fresh 0.5%Pt/ZrO_2 catalyst and (B) spent 0.5%Pt/ZrO_2 catalyst

In Figures S14A show the HAADF-STEM-EDX mapping images of the fresh Pt/ZrO_2 catalyst,

and it can be observed that Pt and Zr are dispersed uniformly with no obvious aggregation of Pt. Such a uniform distribution of Pt species likely minimizes the formation of heavy carbonaceous species, thereby improving the selectivity towards C_2 hydrocarbons. Compared with 0.5%Pt/ZrO_2-fresh catalyst, there were no obvious Pt sintering and coke formation for post reaction in HAADF-STEM-EDX analysis on 0.5%Pt/ZrO_2 catalyst, as shown in Figure S14 B.

14. XPS and N_2-physisorption of the fresh and spent Pt/ZrO_2 catalyst

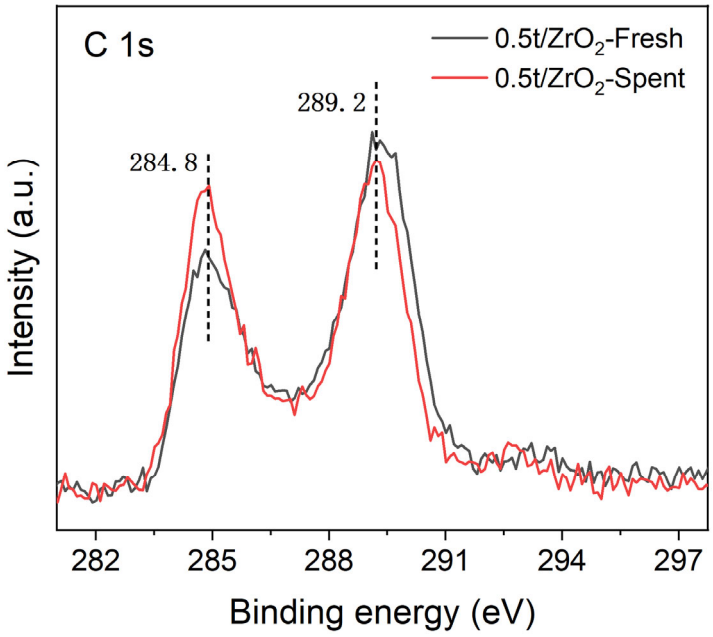

Figure S15.XPS spectra of C 1s for fresh and spent Pt/ZrO_2 catalyst.

As shown in Figure S15, an increase in the intensity of the C1s peak at 284.8 eV typically indicates an increase in the amount of carbon in a graphitic or hydrocarbon-like environment. This could suggest a greater presence of such carbon-containing species on the surface of the sample.

Table S7 Textural properties of 0.5%Pt/ZrO_2 catalyst

Catalyst supports	BET surface area (m^2 g^{-1})	Average pore diameter (nm)	Pore volume (cm^3 g^{-1})
0.5%Pt/ZrO2-Fresh	13.5	32.3	0.0022
0.5%Pt/ZrO2-Spent	12.3	33.4	0.0011

Based on the N_2 physisorption data, as shown in Table S7, the fresh 0.5% Pt/ZrO_2 catalyst has a BET surface area of 13.5 m^2/g, an average pore diameter of 32.3 nm, and a pore volume of 0.0022 cm^3 /g. In contrast, the spent 0.5% Pt/ZrO_2 catalyst has a BET surface area of 12.3 m^2 /g, an average pore diameter of 33.4 nm, and a pore volume of 0.0011 cm^3 /g. The decrease in BET surface area and pore volume for the spent catalyst suggests sintering and agglomeration of the catalyst particles during the reaction. This conclusion is supported by the increase in average pore diameter, indicating that smaller pores have been lost or merged due to the sintering process.

15. Surface Pt and Zr species determined by XPS

Table S8 Relative content of Pt and Zr species in the Pt/ZrO_2 catalysts[a]

Catalysts	Relative surface percentage of Pt and Zr elements/%				
	Pt^0	Pt^{2+}	Pt^{4+}	Zr^{3+}	Zr^{4+}
Pt/ZrO_2-Fresh	18.0	53.7	28.3	17.3	82.7
Pt/ZrO_2-Spent	50.5	43.0	6.5	20.1	79.9

[a] The result was obtained by fitting the XPS peaks.

16. NOCM performances using ZrO_2 packing without Pt

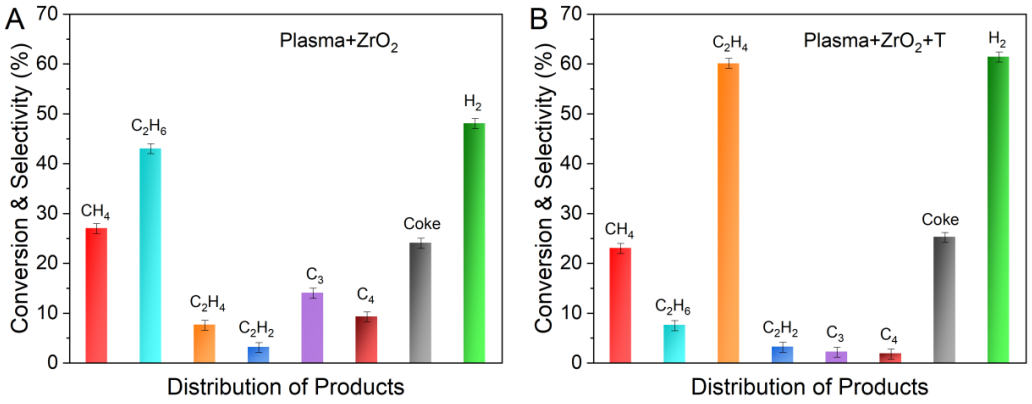

Figure S16. Comparative performance analysis of NOCM in (A) plasma+ZrO_2 system, and (B) plasma+ZrO_2+T system (T represents thermal cracking temperature is 880 °C).

Figure S16 illustrates the CH_4 conversion and product selectivity for NOCM using ZrO_2 packing. In Figure S16A, the selectivity for C_2H_6 is approximately 43%, while in Figure S16B, the selectivity for C_2H_4 is around 61.4%. These values are comparable to those observed in the plasma alone system (Figure 1A of the main paper) and the plasma+T system (Figure 1C of the main paper). These results indirectly demonstrate that the improvements in selectivity for C_2H_6 and C_2H_4 are primarily attributed to the presence of Pt sites rather than the ZrO_2 packing. ZrO_2 serves as an excellent support, enhancing the stability and dispersion of Pt.[23-25] The stable Pt improves catalytic efficiency and reaction selectivity, particularly in the conversion CH_4 to C_2H_6. ethylene is primarily obtained from the thermal cracking of alkanes in Stage 2. When the Pt/ZrO_2 catalyst is introduced in the Stage 1 DBD plasma, it increases the yield of ethane, leading to a higher production of C_2H_4 throughout the two-stage system. The coordinatively unsaturated Pt sites are more active for C-H bond scission because electrons from Pt are transferred to the C-H anti-bonding orbital of CH_4. This electron transfer weakens the C-H bond and lowers the barrier for C-H bond dissociation, thereby facilitating CH_4 cracking and enhancing CH_4 conversion.[26]

17. OES measurement and calculation of electron density

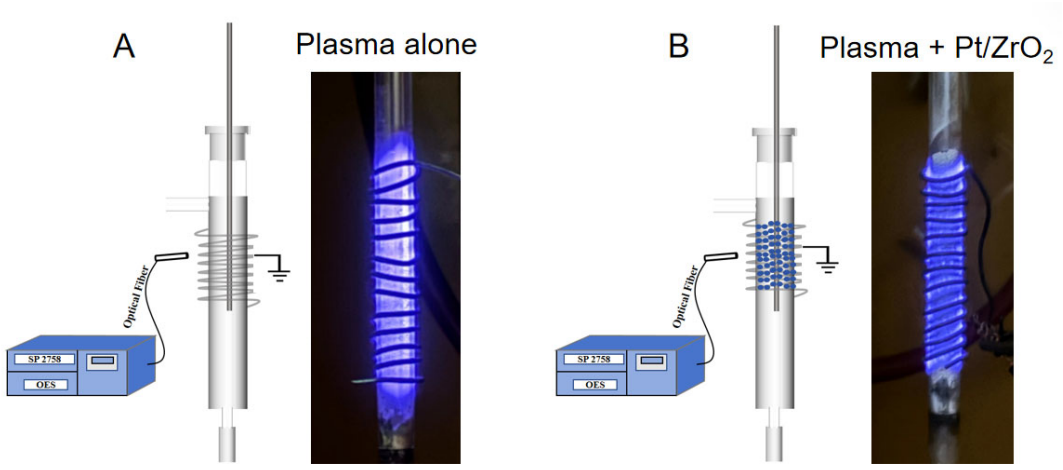

Figure S17. The schematic of the OES measurement.

Figure S17 illustrates the schematic of the OES measurement. The N_2 second positive system observed in the spectra can be attributed to the micro-discharges of air occurring at the external grounding electrode. In the plasma alone system, the discharge emission intensity is higher due to the absence of a catalyst, resulting in stronger optical signal collection. Consequently, the N_2-SPS peaks in Figure 3C (plasma alone system) exhibit greater intensity compared to the Figure 3D (plasma+Pt/ZrO_2 system).

The electron density in NOCM was compared by the line-ratio method of optical emission spectroscopy (OES) for plasma alone and plasma + Pt/ZrO_2 system, as shown in Table S9. According to the collisional-radiative model,[27] there is a specific relationship between these spectral line ratios and the electron density.

$$\frac{I_1}{I_2} = \frac{A_1 n_1}{A_2 n_2}$$

Here I_1 and I_2 are the intensities of emission lines in *2p–1s* transitions, $\mathbf{A_1}$ and $\mathbf{A_2}$ are the Einstein coefficients and n_1 and n_2 are the densities of two different 2p levels.

Table S9. Parameters for the electron density line-ratio method of optical emission spectroscopy

	plasma alone (I)	plasma+Pt/ZrO_2 (I)	Einstein coefficients (s^{-1})
Ar_{738} ($2P_3$-$1S_4$)	3915	3162	8.50×10^6
Ar_{750} ($2P_1$-$1S_2$)	14030	10997	4.50×10^7
Ar_{763} ($2P_6$-$1S_5$)	9541	7521	2.45×10^7

According to the literature,[27] The electron density increases with decreasing the R13 (n_{2p1}/n_{2p3}) and increasing the R36 (n_{2p3}/n_{2p6}).

In plasma alone system:

$$R_{13} = \frac{n_{2p1}}{n_{2p3}} = \frac{I_{750} \times A_{738}}{I_{738} \times A_{750}} = \frac{14030 \times 8.50 \times 10^6}{3915 \times 4.50 \times 10^7} = 0.681$$

$$R_{36} = \frac{n_{2p3}}{n_{2p6}} = \frac{I_{738} \times A_{763}}{I_{763} \times A_{738}} = \frac{3915 \times 2.45 \times 10^7}{9541 \times 8.50 \times 10^6} = 1.186$$

In plasma+Pt/ZrO_2 system:

$$R_{13} = \frac{n_{2p1}}{n_{2p3}} = \frac{I_{750} \times A_{738}}{I_{738} \times A_{750}} = \frac{10997 \times 8.50 \times 10^6}{3162 \times 4.50 \times 10^7} = 0.661$$

$$R_{36} = \frac{n_{2p3}}{n_{2p6}} = \frac{I_{738} \times A_{763}}{I_{763} \times A_{738}} = \frac{3162 \times 2.45 \times 10^7}{7521 \times 8.50 \times 10^6} = 1.215$$

Therefore, the electron density of plasma + Pt/ZrO_2 system (R13=0.661, R36=1.215) is higher than that of plasma alone system (R13=0.681, R36=1.186). This indicates that the addition of the Pt/ZrO_2 catalyst is more conducive to CH_4 conversion, which is consistent well with the experiment result.

18. Mean electron energy and electron energy distribution function

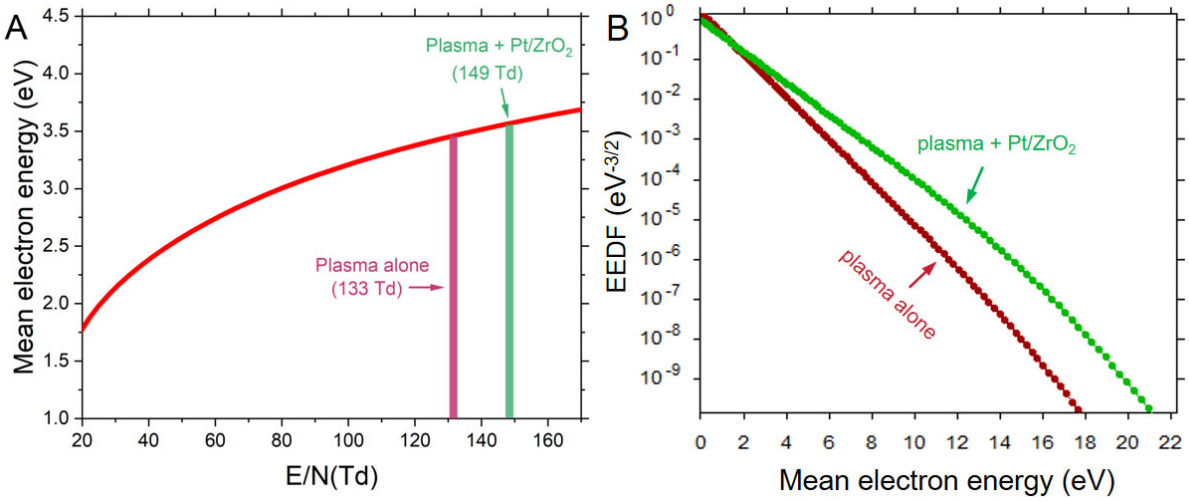

Figure S18. (A) Calculated mean electron energy as a function of reduced electric field (E/N); (B) Electron energy distribution function (EEDF).

Figure S18(A) shows the mean electron energy as a function of the reduced electric field for both the plasma alone system and the plasma+Pt/ZrO_2 system. Compared to the plasma alone system, the plasma+Pt/ZrO_2 system achieves a higher mean electron energy at a higher reduced electric field. As clearly illustrated in Figure S18(B), the peak of the electron energy distribution function (EEDF) gradually decreases, and the peak position shifts towards higher energy. This indicates that the proportion of electrons with lower energies decreases when Pt/ZrO_2 is present in the plasma reactor. Additionally, the range of the EEDF broadens in plasma+Pt/ZrO_2 system, signifying that more electrons with higher energies are generated in the DBD plasma.

19. *In-Situ* FTIR Reaction Cell

The self-designed reaction cell for *in-situ* FTIR characterization under plasma catalysis conditions is depicted in Figure S19. The surface functional groups of the catalyst and gas molecules were characterized using a Thermo Nicolet iS10 infrared spectrometer equipped with a rapidly recoverable detector containing heavy hydrogen triethylene glycol salts (DTGS). The instrument's resolution was set at 4.0 cm^{-1}, with a scanning range from 4000 to 400 cm^{-1}, and each scan was repeated 64 times. Catalyst samples weighing 0.05 g were initially ground to fine powder in a mortar and pestle, then pressed into self-supporting discs with a diameter of Φ=8 mm, and subsequently placed into the infrared cell fitted with CaF_2 windows. The plasma power source was activated, and the discharge mode was initiated to collect signals. The FTIR cell was heated by the plasma, and a thermocouple was employed to monitor real-time temperature. Operational conditions of the *In situ* FTIR experiments: 286-290 ºC gas temperature in the *in-situ* FTIR reaction cell, 28.2 kV discharge voltage, 10 ml/min CH_4, 10 ml/min Ar.

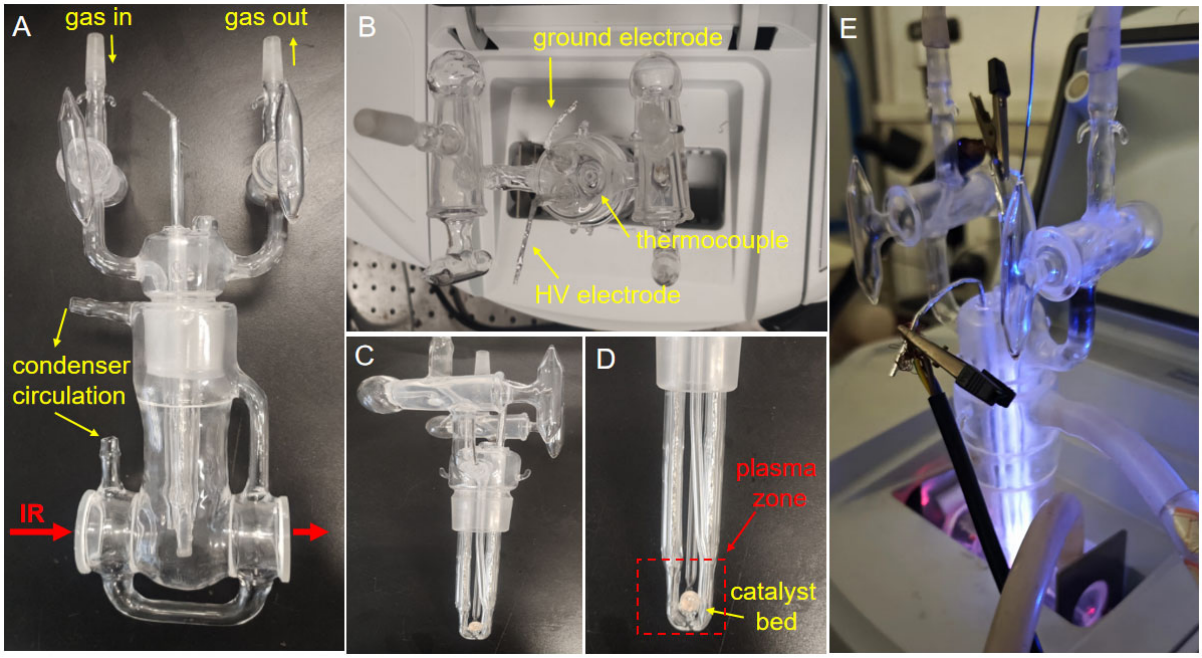

Figure S19. Schematic diagram of the FTIR reaction cell for *in-situ* characterization of plasma catalysis (A) Total image, (B) Position in the Thermo Nicolet iS10 infrared spectrometer, (C) Electrodes of the *in-situ* FTIR reaction cell, (D) Catalyst discs between the high voltage electrode and the grounding electrode, (E) Images of the reaction cell after plasma on.

20. CH_4 conversion and selectivity for pre-reduced Pt/ZrO_2 catalyst

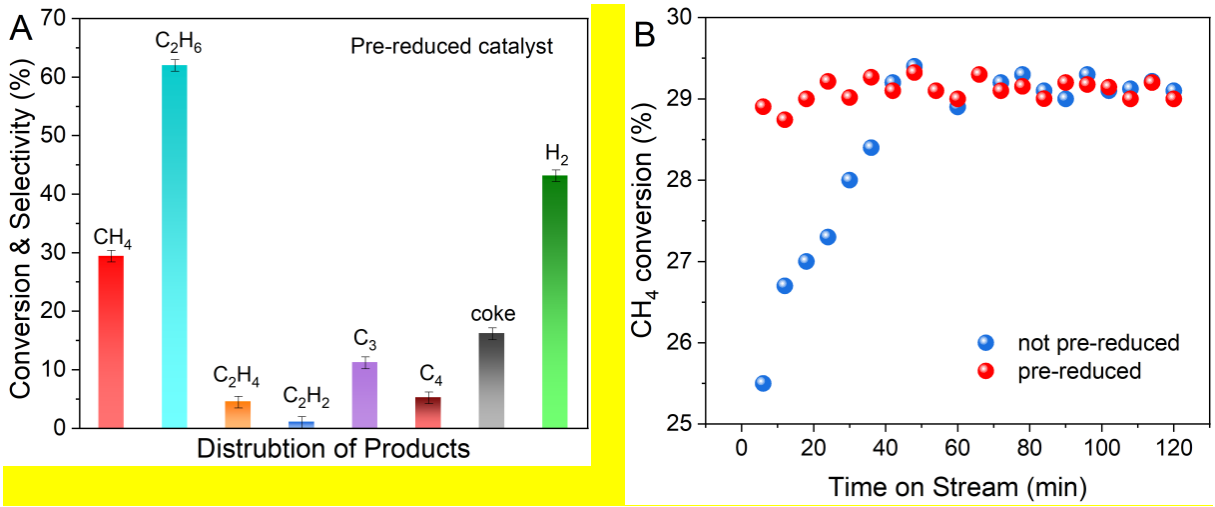

Figure S20. (A) CH_4 conversion and selectivity for pre-reduced Pt/ZrO_2 catalyst, and (B) a comparison for CH_4 conversion between pre-reduced and not pre-reduced in Pt/ZrO_2 catalyst.

Figure S20(A) depicts the steady-state CH_4 conversion and product selectivity of the pre-reduced Pt/ZrO_2 catalyst, which are consistent well with the steady-state results of the catalyst without pre-reduction. The CH_4 conversion of the catalyst without pre-reduction is initially low, as shown in Figure S20(B). However, as the reaction progresses, PtO is gradually reduced, which leads to an increase in CH_4 conversion. This indicates that the catalyst requires a gradual reduction process and further confirms that metallic Pt is the active site in the NOCM reaction.

21. Thermal cracking of C_2H_6, C_3H_8 and C_4H_{10}.

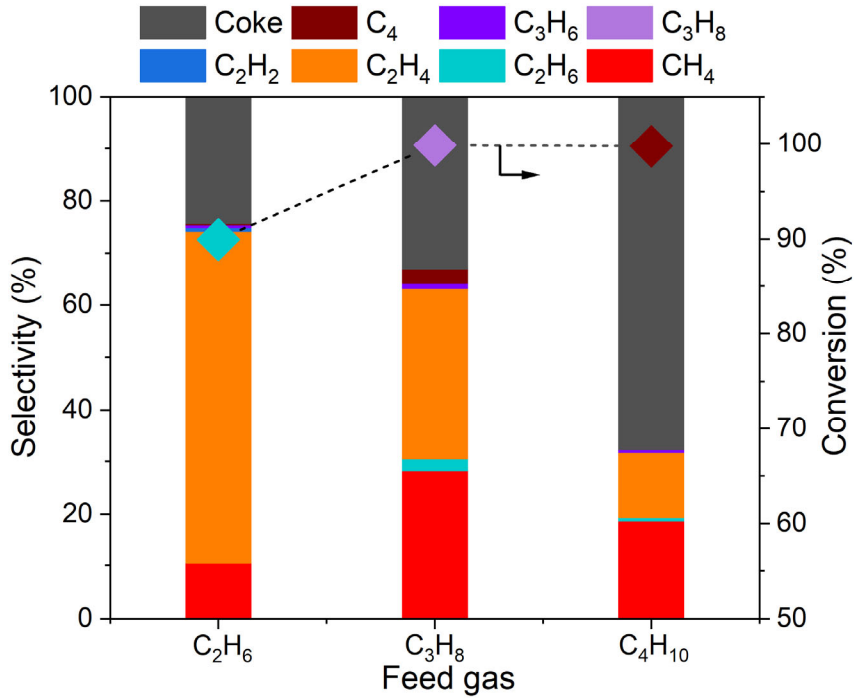

Figure S21. Thermal cracking of C_2H_6, C_3H_8 and i-C_4H_{10} at 880 °C.

Figure S21 shows the conversion and product selectivity in case of C_2H_6, C_3H_8, and i-C_4H_{10} thermal cracking at 880 °C. It clearly demonstrates that the main product in C_2H_6 thermal cracking is C_2H_4. In case of C_3H_8 thermal cracking, C_2H_4 remains the primary product, followed by CH_4. For C_4H_{10} thermal cracking, the main product is CH_4, with C_2H_4 being the second most abundant. Besides, coking becomes gradually more important for the larger cracking. Overall, in the thermal cracking of alkanes, the primary product is C_2H_4, followed by CH_4. Therefore, the CH_4 conversion in the hybrid plasma-thermal system is lower than in the plasma alone system.

References

[1] P.-A. Maitre, J. Long, M.S. Bieniek, M.N. Bannerman, P.N. Kechagiopoulos, Investigating the effects of helium, argon and hydrogen co-feeding on the non-oxidative coupling of methane in a dielectric barrier discharge reactor, Chemical Engineering Science 259 (2022). https://doi.org/10.1016/j.ces.2022.117731.

[2] S. Jo, H. Lee Dae, Y.-H. Song, Product analysis of methane activation using noble gases in a non-thermal plasma, Chemical Engineering Science 130 (2015) 101-108. https://doi.org/10.1016/j.ces.2015.03.019.

[3] S. Jo, D. Hoon Lee, W. Seok Kang, Y.-H. Song, Methane activation using noble gases in a dielectric barrier discharge reactor, Physics of plasmas 20(8) (2013). https://doi.org/10.1063/1.4818795.

[4] D. Gerceker, A.H. Motagamwala, K.R. Rivera-Dones, J.B. Miller, G.W. Huber, M. Mavrikakis, J.A. Dumesic, Methane Conversion to Ethylene and Aromatics on PtSn Catalysts, Acs Catalysis 7(3) (2017) 2088-2100. https://doi.org/10.1021/acscatal.6b02724.

[5] K. Dutta, V. Chaudhari, C.-J. Li, J. Kopyscinski, Methane conversion to ethylene over GaN catalysts. Effect of catalyst nitridation, Applied Catalysis A: General (2020). https://doi.org/10.1016/j.apcata.2020.117430.

[6] H. Sheng, E.P. Schreiner, W. Zheng, R.F. Lobo, Non-oxidative Coupling of Methane to Ethylene Using Mo2C/[B]ZSM-5, Chemphyschem 19(4) (2017) 504-511. https://doi.org/10.1002/cphc.201701001.

[7] D. Bajec, A. Kostyniuk, A. Pohar, B. Likozar, Nonoxidative methane activation, coupling, and conversion to ethane, ethylene, and hydrogen over Fe/HZSM-5, Mo/HZSM-5, and Fe-Mo/HZSM-5 catalysts in packed bed reactor, International Journal of Energy Research 43(13) (2019) 6852-6868. https://doi.org/10.1002/er.4697.

[8] S. Jo, T. Kim, H. Lee Dae, S. Kang Woo, Y.-H. Song, Effect of the Electric Conductivity of a Catalyst on Methane Activation in a Dielectric Barrier Discharge Reactor, plasma Chemistry and plasma Processing 34(1) (2014) 175-186. https://doi.org/10.1007/s11090-013-9505-1.

[9] Y. Ma, X. Han, S. Xu, Z. Li, W. Lu, B. An, D. Lee, S. Chansai, A.M. Sheveleva, Z. Wang, Y. Chen, J. Li, W. Li, R. Cai, I. da Silva, Y. Cheng, L.L. Daemen, F. Tuna, E.J.L. McInnes, L. Hughes, P. Manuel, A.J. Ramirez-Cuesta, S.J. Haigh, C. Hardacre, M. Schröder, S. Yang, Direct Conversion of Methane to Ethylene and Acetylene over an Iron-Based Metal–Organic Framework, Journal of the American Chemical Society 145(38) (2023) 20792-20800. https://doi.org/10.1021/jacs.3c03935.

[10] R. Liu, Y. Hao, T. Wang, L. Wang, A. Bogaerts, H. Guo, Y. Yi, Hybrid plasma-thermal system for methane conversion to ethylene and hydrogen, Chemical Engineering Journal 463 (2023). https://doi.org/10.1016/j.cej.2023.142442.

[11] Y.V.S. M. V. Tsodikov, V. P. Mordovin, O. V. Bukhtenko, G. Colón, M. C. Hidalgo and J. A. Navío, Low temperature selective methane activation to alkenes by a new hydrogen-accumulating system, Chem. Commun. (1999) 943-944.

[12] S.D. Lina Liu, Zhikun Zhang, and Sibudjing Kawi, Nonoxidative Coupling of Methane over Ceria-Supported SingleAtom Pt Catalysts in DBD plasma, ACS Appl. Mater. Interfaces 14 (2022) 5363-5375. https://doi.org/10.1021/acsami.1c21550.

[13] X. Guo, G. Fang, G. Li, H. Ma, H. Fan, L. Yu, C. Ma, X. Wu, D. Deng, M. Wei, D. Tan, R. Si, S. Zhang, J. Li, L. Sun, Z. Tang, X. Pan, X. Bao, Direct, Nonoxidative Conversion of Methane to Ethylene, Aromatics, and Hydrogen, Science 344 (2014) 616-619.

[14] O.B. Ayodele, Resolving one of the holy grails of catalysis: Direct nonoxidative methane conversion to ethylene over plasma-assisted atomically dispersed Pt catalyst, International Journal of Hydrogen Energy 47(98) (2022) 41527-41539. https://doi.org/10.1016/j.ijhydene.2021.12.200.
[15] Goodwin DG, Moffat HK, Schoegl I, Speth RL, Weber BW., Cantera: An Object-oriented Software Toolkit for Chemical Kinetics, Thermodynamics, and Transport Processes 2023. https://doi.org/10.5281/zenodo.8137090.
[16] McBride BJ, Zehe MJ, Gordon S. NASA Glenn coefficients for calculating thermodynamic properties of individual species. Clevelend, OH, USA: NASA Glenn Research Center; 2002.
[17] Smith WR, Missen RW. Chemical reaction equilibrium analysis: Theory and algorithms. New York, NY, USA: Wiley; 1982.
[18] C. De Bie, B. Verheyde, T. Martens, J. van Dijk, S. Paulussen, A. Bogaerts, Fluid Modeling of the Conversion of Methane into Higher Hydrocarbons in an Atmospheric Pressure Dielectric Barrier Discharge, plasma Processes and Polymers 8(11) (2011) 1033-1058. https://doi.org/10.1002/ppap.201100027.
[19] M. Scapinello, E. Delikonstantis, G.D. Stefanidis, Direct methane-to-ethylene conversion in a nanosecond pulsed discharge, Fuel 222 (2018) 705-710. https://doi.org/10.1016/j.fuel.2018.03.017.
[20] E. Delikonstantis, M. Scapinello, D. Stefanidis Georgios, Low energy cost conversion of methane to ethylene in a hybrid plasma-catalytic reactor system, Fuel Processing Technology 176 (2018) 33-42. https://doi.org/10.1016/j.fuproc.2018.03.011.
[21] M.S. Evangelos Delikonstantis, Orelie Van Geenhoven, Georgios D. Stefanidis, Nanosecond pulsed discharge-driven non-oxidative methane coupling in a plate-to-plate electrode configuration plasma reactor, Chemical Engineering Journal 380 (2020) 122477. https://doi.org/10.1016/j.cej.2019.122477.
[22] B. Huang, C. Zhang, H. Bai, S. Zhang, K. Ostrikov, T. Shao, Energy pooling mechanism for catalyst-free methane activation in nanosecond pulsed non-thermal plasmas, Chemical Engineering Journal 396 (2020). https://doi.org/10.1016/j.cej.2020.125185.
[23] K. Liu, T. Zhang, X. Liu, T. Wang, Y. Su, H. Wang, L. Sun, X. Cao, Y. Bi, K. Wang, L. Zhang, Influence of reduction temperature on Pt–ZrO2 interfaces for the gas-phase hydrogenation of acetone to isopropanol, Catalysis Science & Technology 13(9) (2023) 2675-2684. https://doi.org/10.1039/d2cy02139k.
[24] R. Torralba, G. Corro, F. Rosales, F. Bañuelos, U. Pal, O. Olivares-Xometl, E. Guilleminot, J.L.G. Fierro, Total Oxidation of Methane Over Sulfur Poisoning Resistant Pt/ZrO2 Catalyst: Effect of Pt2+–Pt4+ and Pt2+–Zr4+ Dipoles at Metal-Support Interface, Catalysis Letters 151(6) (2020) 1592-1603. https://doi.org/10.1007/s10562-020-03411-9.
[25] L. Zhu, J.-Q. Lu, P. Chen, X. Hong, G.-Q. Xie, G.-S. Hu, M.-F. Luo, A comparative study on Pt/CeO2 and Pt/ZrO2 catalysts for crotonaldehyde hydrogenation, Journal of Molecular Catalysis A: Chemical 361-362 (2012) 52-57. https://doi.org/10.1016/j.molcata.2012.05.002.
[26] Y. Wang, P. Hu, J. Yang, Y.A. Zhu, D. Chen, C-H bond activation in light alkanes: a theoretical perspective, Chem Soc Rev 50(7) (2021) 4299-4358. https://doi.org/10.1039/d0cs01262a.
[27] X.M. Zhu, Y.K. Pu, N. Balcon, R. Boswell, Measurement of the electron density in atmospheric-pressure low-temperature argon discharges by line-ratio method of optical emission spectroscopy, Journal of Physics D: Applied Physics 42(14) (2009). https://doi.org/10.1088/0022-3727/42/14/142003.